Supporting Information for

Dipole modelling for a robust description of subdiffractional polariton waves

Flávio H. Feres[1,2], Ingrid D. Barcelos[1], Rafael A. Mayer[1,3], Thiago M. dos Santos[1], Raul O. Freitas[1], Markus B. Raschke[4], Dario A. Bahamon[5] and Francisco C. B. Maia[1,*]

1 - Brazilian Synchrotron Light Laboratory (LNLS), Brazilian Center for Research in Energy and Materials (CNPEM), Zip Code 13083-970, Campinas, Sao Paulo, Brazil.

2 - Physics Department, Institute of Geosciences and Exact Sciences, São Paulo State University – UNESP, Rio Claro 13506-900, Brazil

3 – Physics Department, Gleb Wataghin Physics Institute, University of Campinas (Unicamp), 13083-859 Campinas, São Paulo, Brazil

4 - Department of Physics, Department of Chemistry, and Joint Institute for Lab Astrophysics (JILA), University of Colorado, Boulder, Colorado 80309, United States.

5 - MackGraphe - Graphene and Nanomaterials Research Center, Mackenzie Presbyterian University, 01302-907, São Paulo, Brazil

*Corresponding author: francisco.maia@lnls.br

1. The dielectric tensor of hexagonal boron nitride

The hexagonal boron nitride[1] nanometer-sized crystal used in this work are uniaxial van der Waals crystals with the crystalline axes a, b and c shown in Figure S1. In the a-b plane, the crystal presents atomically thick planes of hexagons of boron and nitrogen covalently bonded. Along the c axis, which is the optical axis, those planes are juxtaposed and held together by van der Waals forces. Due to this crystalline structure, its dielectric tensor $\overleftrightarrow{\varepsilon}$(Equation S1) is isotropic in the a-b plane and anisotropic along the c axis. Hence, hBN crystal is, commonly, classified isotropic in-plane and anisotropic out-of-plane. Therefore, thein-plane components of $\overleftrightarrow{\varepsilon}$ can be labeled as $\varepsilon_{aa} = \varepsilon_{bb} = \varepsilon_{\perp}$ and, the out-of-plane ones, as $\varepsilon_{cc} = \varepsilon_{\parallel}$. As conventionally adopted the symbols $\perp$ and $\parallel$ indicate perpendicular and parallel directional with respect to the optical axis c.

$$\overleftrightarrow{\varepsilon} = \begin{bmatrix} \varepsilon_{aa} & 0 & 0 \\ 0 & \varepsilon_{bb} & 0 \\ 0 & 0 & \varepsilon_{cc} \end{bmatrix} \qquad \text{(S1)}$$

In the range from $\omega_{TO,\parallel}$ = 746 cm^{-1} to $\omega_{LO,\parallel}$ = 819 cm^{-1}, hBN presents the type I hyperbolic band containing the out-of-plane polarized phonons. In the range $\omega_{TO,\perp}$ = 1365 cm^{-1} to $\omega_{LO,\perp}$ = 1610 cm^{-1}, type II hyperbolic band appears associated with the in-plane polarized phonons. In general, $\varepsilon_{\parallel}$ and $\varepsilon_{\perp}$ are given by the Lorentzian functions[1,2] in the Equation S2.

$$\varepsilon_{\alpha}(\omega) = \varepsilon_{\infty,\alpha}\left(1 + \frac{\omega_{LO,\alpha}^{2} - \omega_{TO,\alpha}^{2}}{\omega_{TO,\alpha}^{2} - \omega^{2} - i\omega\Gamma_{\alpha}}\right), \qquad \alpha = \perp, \parallel \qquad \text{(S2)}$$

In Equation S2, $\varepsilon_{\infty\perp}$ = 4.9 and $\varepsilon_{\infty\parallel}$ = 2.95 are the asymptotic intrinsic dielectric amplitudes for high frequencies, $\Gamma_{\perp}$ = 5 cm^{-1} and $\Gamma_{\parallel}$ = 4 cm^{-1}are the dielectric damping for each component.

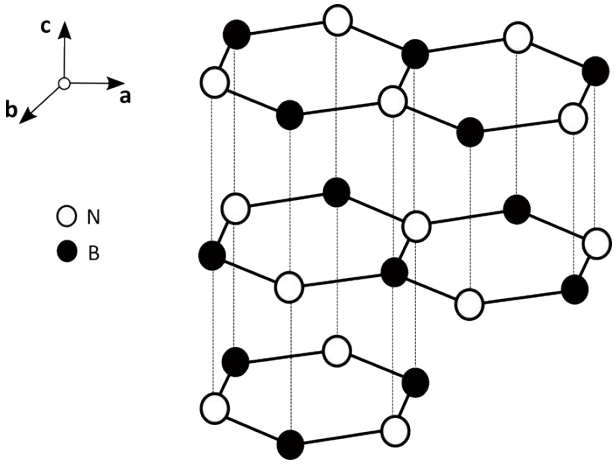

Figure S1- Hexagonal boron nitride lattice. The covalently N-B hexagons lie on a-b planes that are juxtaposed along the c axis.

2. Dielectric function of gold (Au)

We use the dielectric function of Au given from ref. 3 that assumes the Drude-Sommerfeld free electron mode given by Equation S3, where: ω_p= 8.45 eV/$\hbar$ is the plasmonic frequency and $\Gamma_{Au} = {}^{1}/_{\tau_D}$ is the electron relaxation rate, with τ_D = 14 ps.

$$\varepsilon_{Au}(\omega) = 1 - \frac{\omega_p^2}{\omega^2 + i\omega\Gamma_{Au}} \qquad \text{(S3)}$$

3. The electric field of an irradiating dipole

As described in the main text, the crystal edge and the tip, the polariton launchers[5,6] in the hBN/Au system, are replaced by a dipole distribution and by a single dipole, respectively. The superposition of the electric fields irradiated from those dipoles and a non-local (non-propagating) field produce the observed polaritonic field.

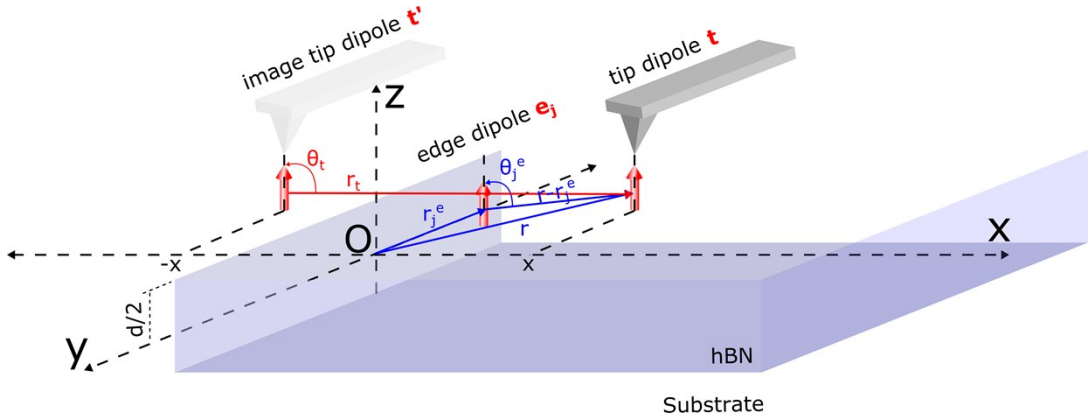

Figure S2- Hertzian Dipole scheme on hBN crystal

The analytic expression of the irradiated electric fields of a single dipole can be derived from the Maxwell equations considering q vector potential[4] (Equation S4). The vector potential can be understood as a consequence of the induced dipolar momentum $\vec{p}$ to the hBN crystal because of the resonant IR illumination.

$$\vec{A}(r) = -iA\frac{e^{-ikr}}{4\pi r}\vec{p} \qquad \text{(S4)}$$

Accordingly, the magnetic field [$\vec{H}(r)$] created by $\vec{p}$ is given by

$$\vec{H}(r) = \frac{1}{\mu}\vec{\nabla} \times \vec{A} \quad \text{(S5)}$$

Where μ is the magnetic permeability of the medium, in the case $\mu = 1$. The electric field $\vec{E}(r)$ outside the source is

$$\vec{E}(r) = i\frac{Z}{k}\vec{\nabla} \times \vec{H} \quad \text{(S6)}$$

Where Z is the impedance of the medium. Therefore, solving the equations S5 and S6, the general expression for a HDA electric field[4] $\vec{E}$ is shown by the Equation S7.

$$\vec{E} = i\frac{kAe^{-ikr}}{4\pi r}\left[\left(\frac{1}{ikr} + \frac{1}{(ikr)^2}\right)2\cos\theta\hat{r} + \left(1 + \frac{1}{ikr} + \frac{1}{(ikr)^2}\right)\sin\theta\hat{\theta}\right] \quad \text{(S7)}$$

$$\vec{e}_z = -iA\frac{ke^{-ikr}}{4\pi r}\sin^2\theta\hat{z} \quad \text{(S8)}$$

In Equation S7, k is the polariton momentum, A is the dipole amplitude and r, the distance from the center of the dipole to a given point. As discussed in the main text, we consider only the z-component $\vec{E}$ in the radiation field regime (Figure S2). The general expression of the $\vec{e}_z$ is shown in Equation S8.

4. The Hertzian dipole model

As discussed in the main manuscript, the tip-launched waves travel to the edge, there, they are reflected back to the tip. In parallel, edge-launched waves travel straight to the tip. Considering a dipole at the tip location and a discrete dipole distribution along the edge, the resulting HP[2] electric field $\vec{E}_z$, probed at the tip position, is given by the Equation S9. The first and the second terms of this equation correspond to the electric fields irradiated from the tip dipole (labeled with subscripts t) and the dipole distribution at the edge (e) with amplitudes A_t and B_j, respectively. The third is the non-propagating field. Regarding the reference frame of the Figure S2 and considering the unit vector $\hat{z}$: $\left|\vec{r} - \vec{r}_j^e\right| = \sqrt{(y - y_e)^2 + \left(d/2\right)^2 + (x)^2}$ and $\theta_j^e = \cos^{-1}\left(\frac{\hat{z}\cdot\left(\vec{r} - \vec{r}_j^e\right)}{\left|\vec{r} - \vec{r}_j^e\right|}\right)$, for the edge, $\left|\vec{r}_t\right| = \sqrt{(y - y_e)^2 + \left(d/2\right)^2 + (2x)^2}$ and $\theta_t = \cos^{-1}\left(\frac{\hat{z}\cdot\vec{r}_t}{\left|\vec{r}_t\right|}\right)$, for the tip. For the sake of completeness, the electric field of the tip dipole has an arbitrary phase difference φ; this extra phase can be understood as different reaction times of the two dipole types to the far-field excitation. .

$$E_z(r) = -ikA\frac{e^{-ik(|\vec{r}_t| + \phi)}}{4\pi|\vec{r}_t|}\sin^2\theta_t - \sum_{j=1}^{N} ikB_j\frac{e^{-ik|\vec{r}-\vec{r}_j^e|}}{4\pi|\vec{r}-\vec{r}_j^e|}\sin^2\theta_j^e + Ce^{-i\alpha} \quad \text{(S9)}$$

5. HDA analysis of HP²s in hBN/SiO_2

The HDA consistency is also demonstrated by the analyses of HP² modes in a 95 nm thick hBN crystal lying on SiO_2 (Figure S3). It is worthy commenting that the hBN/SiO_2 system has been largely investigated in the literature[2,7,8].The spectral linescan amplitude and phase in Figure S3a and S3b, respectively, reveal the characteristic polariton branches in the type II band. For this sample, polariton waves of type I are, vanishingly, small. Using the same procedure reported in main text, we fit to Equation S6 the wave profiles taken from the linescan amplitude as shown in Figure S4a for ω = 1457 cm^{-1}.The parameters of this fit allows for generating the corresponding phase for ω = 1457 cm^{-1}plotted in Figure S4b with the respective data. Importantly, fitting and generated phase, closely, agree with experiments. Figure S5a shows the fit-extracted and calculated momenta-frequency dispersion relations for hBN/SiO_2. These theoretical curves originate from Equations 2 and 3 of the main manuscript where ε_s is the SiO_2 permittivity[9]. Furthermore, we show in Figure S5b the experimental (blue squares) and theoretical (red line) group velocity (v_g) of the type II HP²pulse. As described in the main manuscript, v_g and the fit-extracted imaginary momenta determine a lifetime (τ) around 0.6 ps, calculated at the central frequency ~ 1450 cm^{-1}, for type II HP²s on SiO_2.The HDA analysis, thereby, explains well the experimental data allowing for the attainment of reliable optical properties of the polaritonic waves.

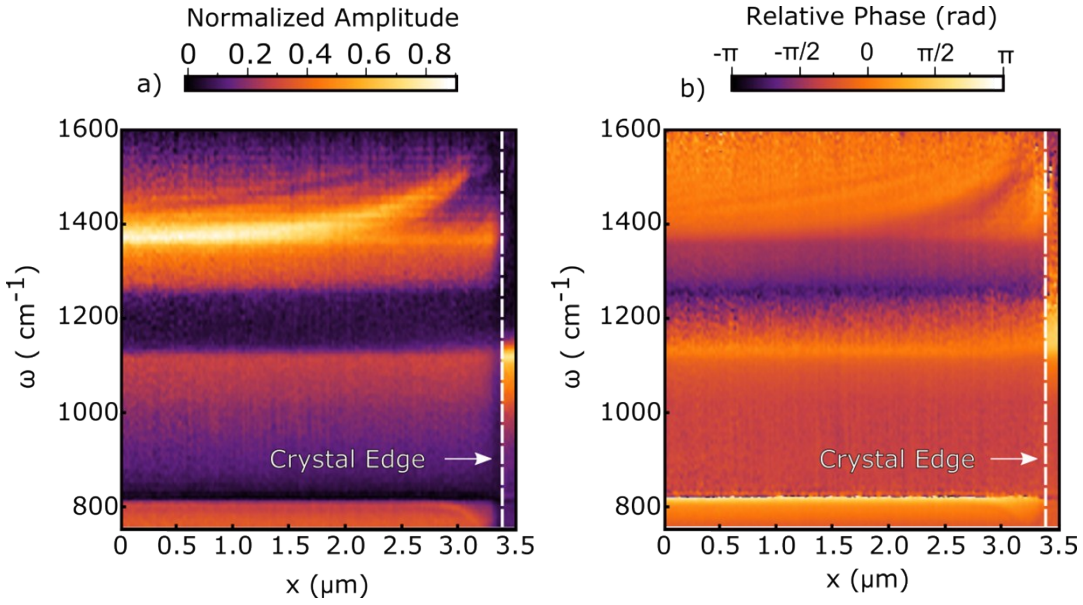

Figure S3- Amplitude a) and relative phase b) obtained from spectral linescan measured in hBN of 95 nm thickness on SiO_2 substrate. The total length of spectral linescan is 3.5 μm: 3.3 μm on the crystal and 0.2 μm on SiO_2.

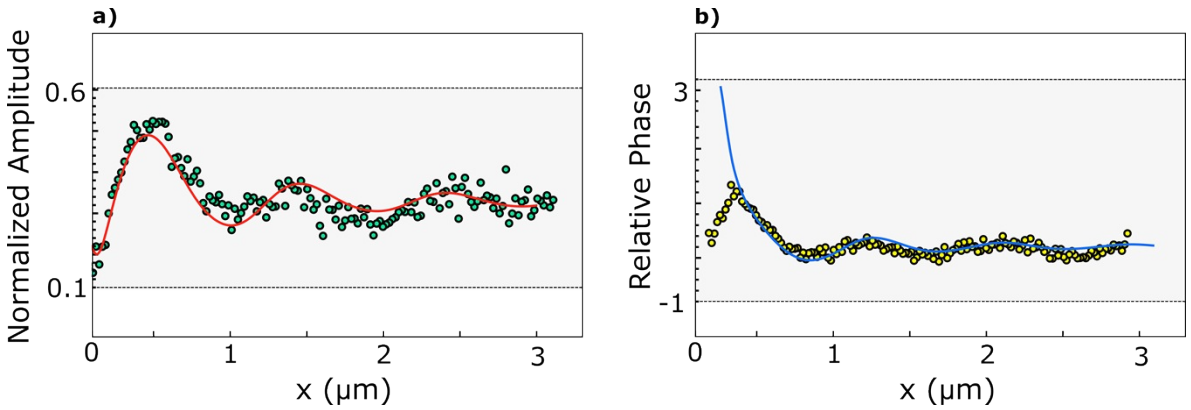

Figure S4 - Fitting using HDA model in HP² waves in hBN measured over SiO_2 substrate. In a) we show the normalized amplitude of the HP² electric field for Type II band with frequency ω = 1457 cm^{-1}, b) relative phase simulated using fit parameters.

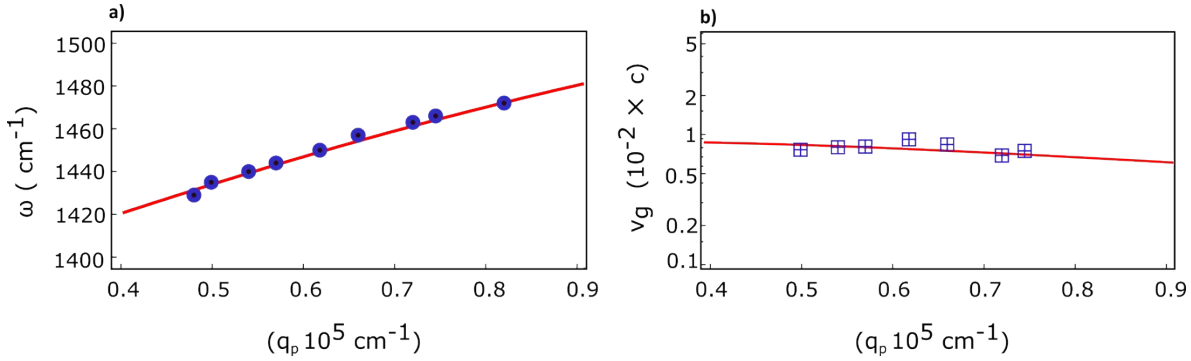

Fig. S5-a) dispersion for type 2 band of hBN over SiO2 substrate, the red continuous line is the dispersion calculated by S.Dai and the blue dots are the momenta extracted by HDA model; b) is the group velocity of the HP² waves, where the red line is the theoretical group velocity and blue square is the fitting group velocity

6. HDA analysis of a 45 nm - thick hBN on Au

Figure S6a and S6b show, respectively, the amplitude and phase of the spectral linescan, across the edge of a 45 nm thick hBN crystal lying on Au substrate, covering the type I band. We note the contrasting polariton branches in both measurements. As performed in the main manuscript, we present in Figure S7a the HDA fits to the polariton profiles, for different ω's, extracted from Figure S6a. The corresponding fit-generated phases are displayed in Figure S7b. Accordingly, theoretical and experimental $\omega - q_p$(Figure S8a) and v_g (Figure S8b) are determined. From those analysis, we find $\tau_p = 1.7\ ps$, for 800 cm^{-1}, and $\tau_p = 1.4\ ps$, for 790 cm^{-1}.

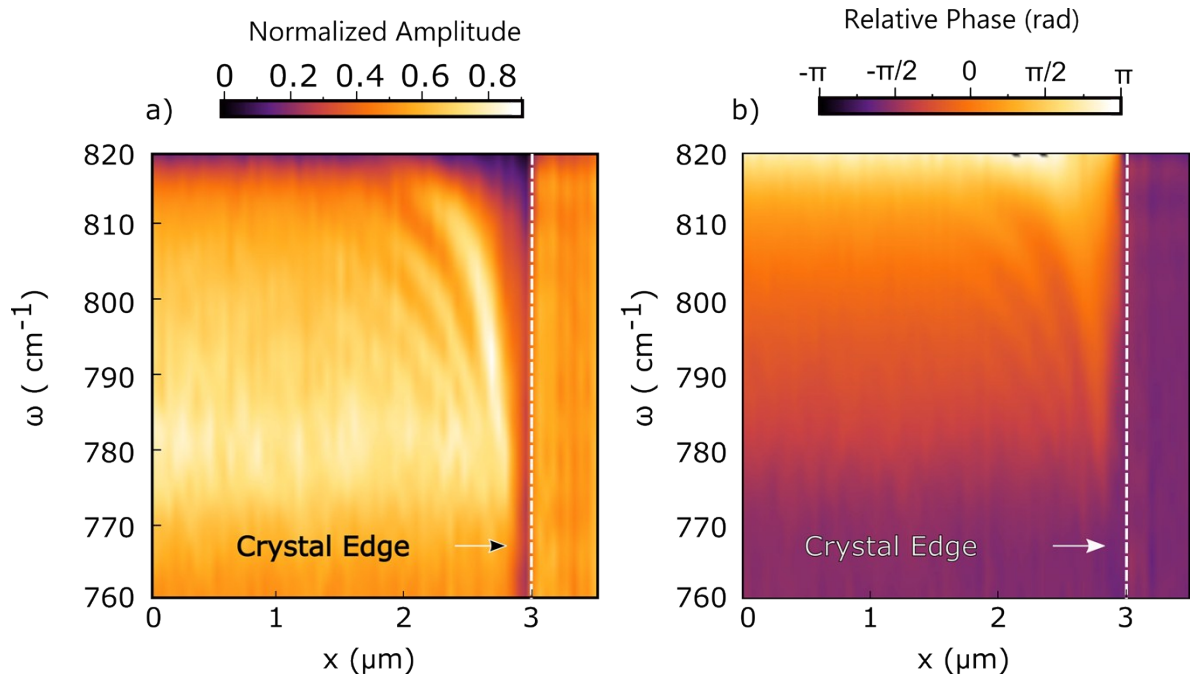

Fig S6-a) amplitude and b) phase of a spectral linescan measured on a 45 nm thick hBN on Au substrate.

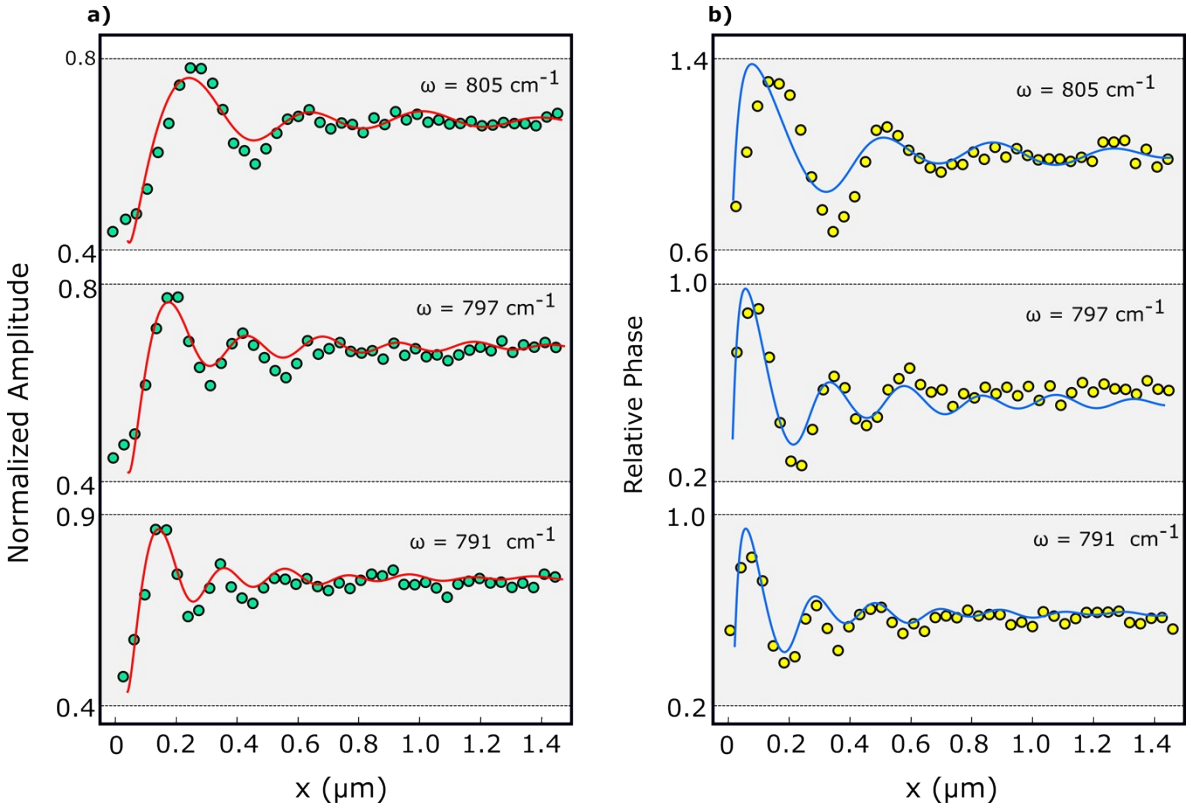

Figure S7- HDA model applied to HP² waves in the 45 nm-thick hBN on Au. a) Fits (red curves) to the experimental polaritons amplitudes (green circles). b) experimental (yellow circles) and fit-generated relative phase (blue curves).

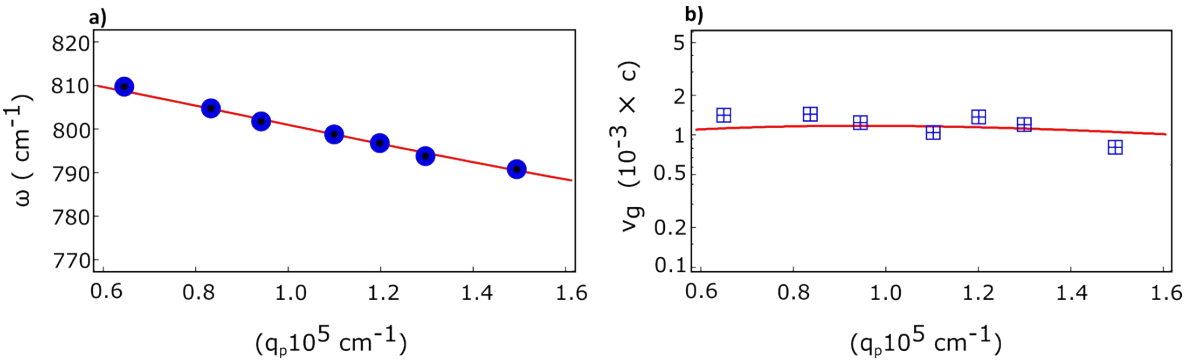

Figure S8- for the type I band of a 45 nm-thich hBN/Au, (a) theoretical (red curve) and experimental (blue circle) $\omega - q_p$ and (b) theoretical (red curve) and experimental (crossed squares) v_g.

7. Comparison between the HDA and previously reported models of polariton waves

We show in Figure S9a-c the fits to type I polariton waves at $\omega = 790\ cm^{-1}$, extracted from Figure 1c of the main text, from our proposed HDA model and from the already reported models in references 10 and 7, respectively. The corresponding fit-generated phases are displayed in Figure S9d-f. We note that only the HDA model enables reconstruction of phase, from the amplitude fit parameters, in reliable agreement with experiment. This model, therefore, exhibits completeness for explaining the complex-valued measurements obtained by SINS and, accordingly, by s-SNOM, as argued in the main text. The analogous examinations, for the type II polaritons, leading to an equivalent conclusion, are presented in Figure S10.

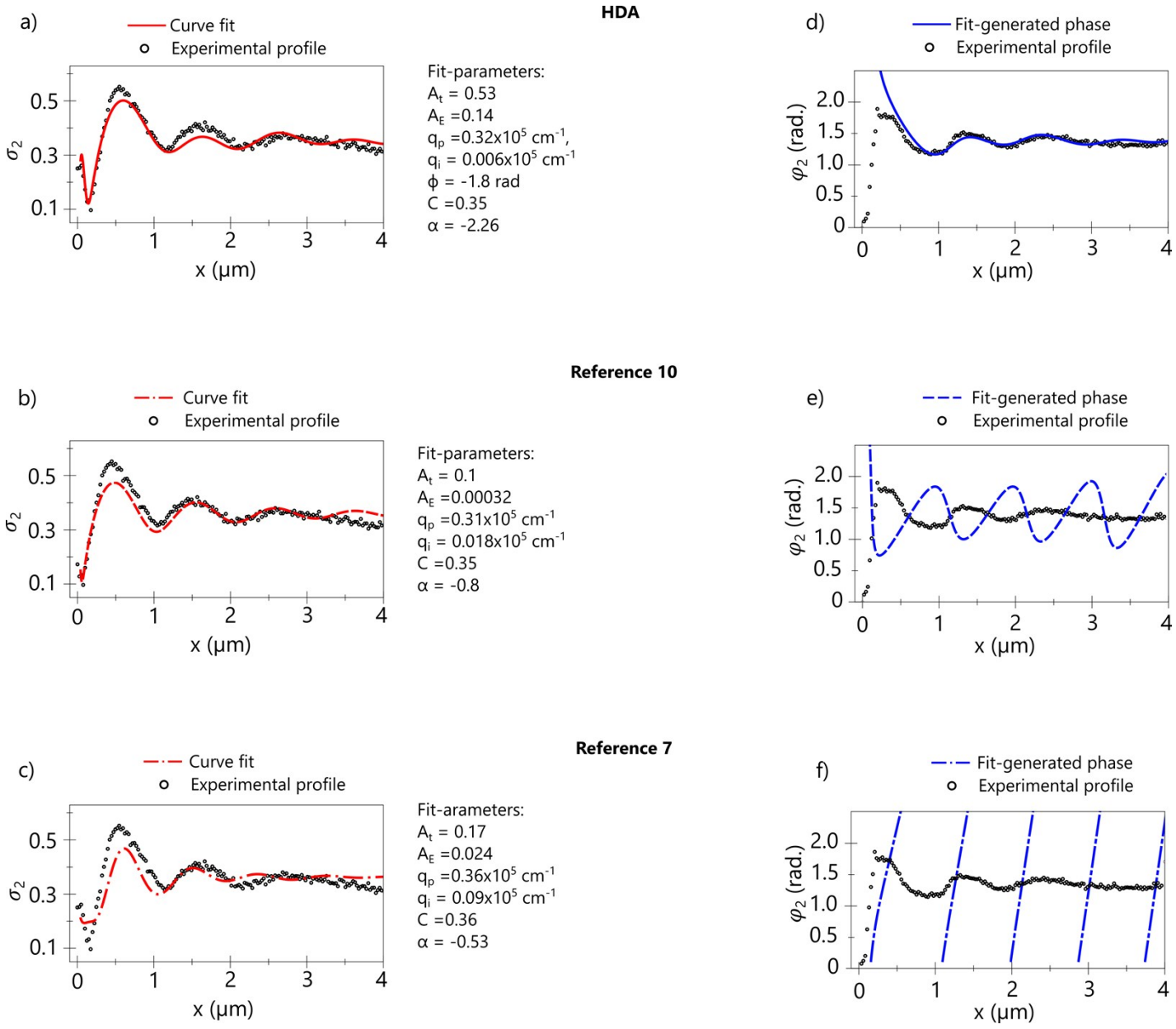

Figure S9 – **a-c**. Fits (red curves) to the amplitude of the type I mode at 795 cm^{-1}, extracted from the measurement shown in Figure 1c of the main text (circles), using the proposed HDA model of this word and models from references 10 and 7, respectively. **d-f**. Corresponding fit-generated phase using the parameters obtained from the fits in **a-c**.

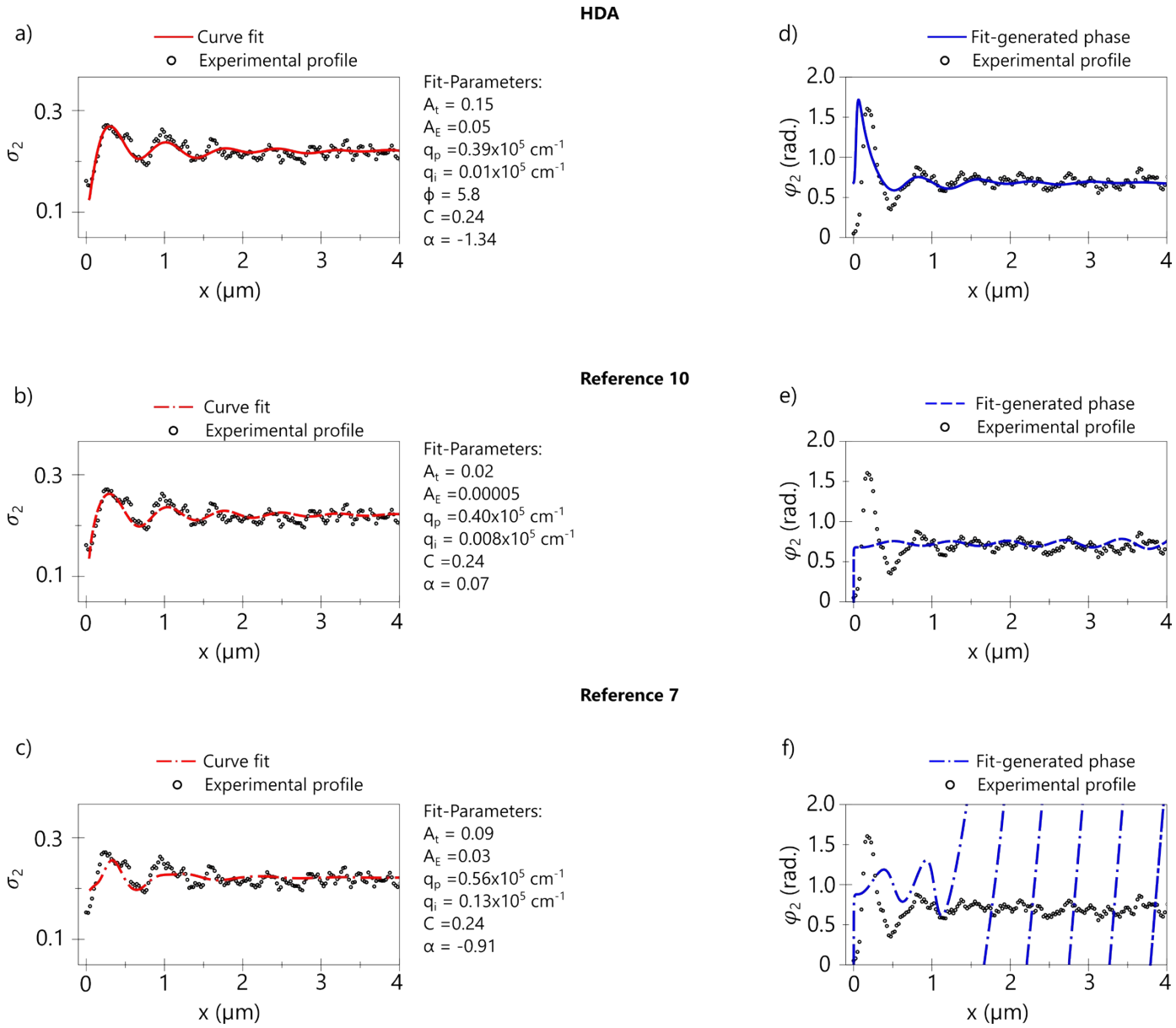

Figure S10 - **a-c**. Fits (red curves) to the amplitude of the type II mode at 1440 cm^{-1}, extracted from the measurement shown in Figure 1e of the main text (circles), using the proposed HDA model of this word and models from references 10 and 7, respectively. **d-f**. Corresponding fit-generated phase using the parameters obtained from the fits in **a-c**.

8. Calculation of the non-local field

To theoretically determine the SINS point-spectrum, we use the standard description of s-SNOM. The tip is polarized by the incident field, which in turn, interacts with the sample via the multiple reflections of the evanescent fields between the tip and the sample. This interaction is embedded in the scattered far field and is proportional to the effective polarizability of the tip (χ). There are different approaches to calculate the effective tip-sample coupling, however, more sophisticated models are required when the reflectivity function $\beta=r_p(\omega,q)$ depends strongly on the in-plane momentum q. Based on the above, we specifically follow the generalized spectral method (GSM) proposed in Ref.[11] , they showed that

the effective polarizability is a functional of the reflectivity and the tip-sample distance (z_{tip}) and can be decomposed into eigenfunctions of an auxiliary problem. For each distance z_{tip} the polarizability can be represented by a series expansion:

$$\chi(\beta) = \sum_{k=0}^{N} \frac{R_k}{\beta_k - \beta} \tag{S10}$$

Further details of the eigenproblem or the method to calculate the poles β_k and the residues R_k can be find in Ref.[11]. It is important to mention that we used a perfect conducting spheroidal probe with curvature radius a = 30 nm and different major semi-axis lengths (L).

Finally, the demodulated signal is calculated by:

$$C(\omega)e^{-i\alpha(\omega)} = [1 + r_p]^2 \left(\int_0^{2\pi} \chi(\omega, z_{tip}) e^{in\varphi} \frac{d\varphi}{2\pi} \right) \tag{S11}$$

Moreover, the hyperspectral images were simulated replacing the non-local field, $C(\omega)e^{-i\alpha(\omega)}$, by the SINS spectra simulation and setting the amplitude of the dipoles as $A_t = 1$ and $A_e = {}^{1}/_{3}$. Thus, the total electric field of the HP² waves is given Equation S9, same as Equation 1 of the main manuscript. For the phase φ, we use values given from fits.

9. References

(1) Dai, S.; Fei, Z.; Ma, Q.; Rodin, A. S.; Wagner, M.; Mcleod, A. S.; Liu, M. K.; Gannett, W.; Regan, W.; Watanabe, K.; et al. Tunable Phonon Polaritons in Atomically Thin van Der Waals Crystals of Boron Nitride. *Science (80-.).* **2014**, *343* (6175), 1125–1129. https://doi.org/10.1126/science.1246833.

(2) Dai, S.; Ma, Q.; Liu, M. K.; Andersen, T.; Fei, Z.; Goldflam, M. D.; Wagner, M.; Watanabe, K.; Taniguchi, T.; Thiemens, M.; et al. Graphene on Hexagonal Boron Nitride as a Tunable Hyperbolic Metamaterial. *Nat. Nanotechnol.* **2015**, *10* (8), 682–686. https://doi.org/10.1038/nnano.2015.131.

(3) Olmon, R. L.; Slovick, B.; Johnson, T. W.; Shelton, D.; Oh, S. H.; Boreman, G. D.; Raschke, M. B. Optical Dielectric Function of Gold. *Phys. Rev. B - Condens. Matter Mater. Phys.* **2012**, *86* (23), 1–9. https://doi.org/10.1103/PhysRevB.86.235147.

(4) Jackson, J. D. *Classical Electrodynamics*, Third Edit.; Wiley.

(5) Yoxall, E.; Schnell, M.; Nikitin, A. Y.; Txoperena, O.; Woessner, A.; Lundeberg, M. B.; Casanova, F.; Hueso, L. E.; Koppens, F. H. L.; Hillenbrand, R. Direct Observation of Ultraslow Hyperbolic Polariton Propagation with Negative Phase Velocity. *Nat. Photonics* **2015**, *9* (9), 674–679. https://doi.org/10.1038/nphoton.2015.166.

(6) Ambrosio, A.; Tamagnone, M.; Chaudhary, K.; Jauregui, L. A.; Kim, P.; Wilson, W. L.; Capasso, F. Selective Excitation and Imaging of Ultraslow Phonon Polaritons in Thin Hexagonal Boron Nitride Crystals. *Light Sci. Appl.* **2018**, *7* (1). https://doi.org/10.1038/s41377-018-0039-4.

(7) Li, P.; Dolado, I.; Alfaro-Mozaz, F. J.; Nikitin, A. Y.; Casanova, F.; Hueso, L. E.; Vélez, S.; Hillenbrand, R. Optical Nanoimaging of Hyperbolic Surface Polaritons at the Edges of van Der Waals Materials. *Nano Lett.* **2017**, *17* (1), 228–235. https://doi.org/10.1021/acs.nanolett.6b03920.

(8) Alfaro-Mozaz, F. J.; Alonso-González, P.; Vélez, S.; Dolado, I.; Autore, M.; Mastel, S.; Casanova, F.; Hueso, L. E.; Li, P.; Nikitin, A. Y.; et al. Nanoimaging of Resonating Hyperbolic Polaritons in Linear Boron Nitride Antennas. *Nat. Commun.* **2017**, *8*, 15624. https://doi.org/10.1038/ncomms15624.

(9) Ni, G. X.; McLeod, A. S.; Sun, Z.; Wang, L.; Xiong, L.; Post, K. W.; Sunku, S. S.; Jiang, B. Y.; Hone, J.; Dean, C. R.; et al. Fundamental Limits to Graphene Plasmonics. *Nature* **2018**, *557* (7706), 530–533. https://doi.org/10.1038/s41586-018-0136-9.

(10) Woessner, A.; Lundeberg, M. B.; Gao, Y.; Principi, A.; Alonso-González, P.; Carrega, M.; Watanabe, K.; Taniguchi, T.; Vignale, G.; Polini, M.; et al. Highly Confined Low-Loss Plasmons in Graphene–Boron Nitride Heterostructures. *Nat. Mater.* **2014**, *14* (4), 421–425. https://doi.org/10.1038/nmat4169.

(11) Jiang, B. Y.; Zhang, L. M.; Castro Neto, A. H.; Basov, D. N.; Fogler, M. M. Generalized Spectral Method for Near-Field Optical Microscopy. *J. Appl. Phys.* **2016**, *119* (5). https://doi.org/10.1063/1.4941343.